6. R. F. Voss, R. A. Webb, *Phys. Rev. Lett.* **47**, 265 (1981).
7. S. Washburn, R. A. Webb, R. F. Voss, S. M. Faris, *Phys. Rev. Lett.* **54**, 2712 (1985).
8. D. B. Schwartz, B. Sen, C. N. Archie, J. E. Lukens, *Phys. Rev. Lett.* **55**, 1547 (1985).
9. J. Clarke, A. N. Cleland, M. H. Devoret, D. Esteve, J. M. Martinis, *Science* **239**, 992 (1988).
10. M. H. Devoret, J. M. Martinis, J. Clarke, *Phys. Rev. Lett.* **55**, 1908 (1985).
11. J. M. Martinis, M. H. Devoret, J. Clarke, *Phys. Rev. Lett.* **55**, 1543 (1985).
12. P. Silvestrini, V. G. Palmieri, B. Ruggiero, M. Russo, *Phys. Rev. Lett.* **79**, 3046 (1997).
13. S. Han, J. Lapointe, J. E. Lukens, *Phys. Rev. Lett.* **66**, 810 (1991).
14. R. Rouse, S. Han, J. E. Lukens, *Phys. Rev. Lett.* **75**, 1614 (1995).
15. S. Han, R. Rouse, J. E. Lukens, *Phys. Rev. Lett.* **76**, 3404 (1996).
16. ———, *Phys. Rev. Lett.* **84**, 1300 (2000).
17. J. R. Friedman, V. Patel, W. Chen, S. K. Tolpygo, J. E. Lukens, *Nature* **406**, 43 (2000).
18. C. H. van der Wal *et al.*, *Science* **290**, 773 (2000).
19. I. I. Rabi, *Phys. Rev.* **51**, 652 (1937).
20. S. Lloyd, *Science* **261**, 1569 (1993).
21. M. F. Bocko, A. M. Herr, M. J. Feldman, *IEEE Trans. Appl. Supercond.* **7**, 3638 (1997).
22. Y. Makhlin, G. Schön, A. Shnirman, *Rev. Mod. Phys.* **73**, 357 (2001).
23. T. H. Stievater *et al.*, *Phys. Rev. Lett.* **87**, 133603 (2001).
24. R. H. Blick, D. W. van der Weide, R. J. Haug, K. Eberl, *Phys. Rev. Lett.* **81**, 689 (1998).
25. C. A. Stafford, N. S. Wingreen, *Phys. Rev. Lett.* **76**, 1916 (1996).
26. A. Schülzgen *et al.*, *Phys. Rev. Lett.* **82**, 2346 (1999).
27. Y. Nakamura, Y. A. Pashkin, J. S. Tsai, *Phys. Rev. Lett.* **87**, 246601 (2001).
28. A. Barone and G. Paterno, *Physics and Applications of the Josephson Effect* (John Wiley and Sons, New York, 1982) pp. 1–14.
29. S. Han, Y. Yu, X. Chu, S. Chu, Z. Wang, *Science* **293**, 1457 (2001).

30. We thank Y. Zhang and S. Li for technical assistance in preparing the experiment. S.H. thanks J. E. Lukens for useful discussions. Supported in part by NSF (DMR-9876874 and EIA-0082499) and by Air Force Office of Scientific Research (AFOSR) (grant F49620-01-1-0439), funded under the Department of Defense University Research Initiative on Nanotechnology (DURINT) program and by the Advanced Research and Development Activity (ARDA).

2 January 2002; accepted 15 March 2002

Ordering of Quantum Dots Using Genetically Engineered Viruses

Seung-Wuk Lee, Chuanbin Mao, Christine E. Flynn, Angela M. Belcher*†

A liquid crystal system was used for the fabrication of a highly ordered composite material from genetically engineered M13 bacteriophage and zinc sulfide (ZnS) nanocrystals. The bacteriophage, which formed the basis of the self-ordering system, were selected to have a specific recognition moiety for ZnS crystal surfaces. The bacteriophage were coupled with ZnS solution precursors and spontaneously evolved a self-supporting hybrid film material that was ordered at the nanoscale and at the micrometer scale into ~72-micrometer domains, which were continuous over a centimeter length scale. In addition, suspensions were prepared in which the lyotropic liquid crystalline phase behavior of the hybrid material was controlled by solvent concentration and by the use of a magnetic field.

Building ordered and defect-free two- and three-dimensional structures on the nanometer scale is essential for the construction of next-generation optical, electronic, and magnetic materials and devices (*1–4*). Traditional assembly approaches have been based on hydrogen bonding, coulombic interactions, and van der Waals forces (*1, 4*). Although a bacterial synthetic method was reported to make monodisperse modified polypeptides (*5*), it has been difficult to tune the layer spacing and structure of conventional synthetic polymers because of their polydisperse chain lengths (*6*). Efforts have been directed toward the use of soft materials to organize inorganic materials at the nanoscale. Protein cages have been used as templates to synthesize nanoscale materials in capsids (*7*). DNA recognition linkers have been successfully used to construct specific gold nanocrystal structures (*8, 9*). ZnS and CdS were nucleated in a lyotropic liquid crystalline medium to make nanowires and nanocrystal superlattice structures by a surfactant assembly pathway (*10*). However, these methods have limitations with respect to length scale and type of inorganic material.

Monodisperse biomaterials that have an anisotropic shape are promising as components of well-ordered structures. Liquid crystalline structures of wild-type viruses (Fd, M13, and TMV) were tunable by controlling the solution concentrations, the solution ionic strength, and the external magnetic fields applied to the solutions (*11–14*). We recently showed that engineered viruses can recognize specific semiconductor surfaces through the method of selection by combinatorial phage display (*15*). These specific recognition properties of the virus can be used to organize inorganic nanocrystals, forming ordered arrays over the length scale defined by liquid crystal formation. We have evolved phage and ZnS precursor solutions to self-assemble highly oriented, self-supporting films. In this system, we can easily modulate both the length of bacteriophage and the type of inorganic materials through genetic modification and selection. Here we report our first effort to direct multi–length scale ordering of quantum dot (QD) hybrid self-supporting biocomposite structures using genetically engineered M13 bacteriophage, viruses with monodisperse size and shape. The resulting QD hybrid film material was ordered at the nanoscale and at the micrometer scale into 72-μm domains. These domains repeated continuously over a centimeter length scale. Moreover, viral suspensions containing ZnS QDs were prepared in which the liquid crystalline phase behaviors of the hybrid material were controlled by solvent concentration and by the use of an applied magnetic field.

The most dominant selected peptide binding motif with specific recognition of ZnS crystal surfaces was isolated through screening of phage display libraries (Fig. 1) (*16, 17*). The screening method selected for binding affinity of a population of random peptides displayed as part of the pIII minor coat protein of M13. Selected peptides were expressed at one end of the M13 virus. The virus had a filamentous shape (~880 nm in length and 6.6 nm in diameter), with the peptide insert measuring 10 nm in length (*11*). The dominant binding motif that emerged after five rounds of selection was termed A7, with an amino acid insert sequence (Cys-Asn-Asn-Pro-Met-His-Gln-Asn-Cys) in which the two cysteine groups formed a disulfide bond, restricting the peptide structure to a constrained loop (*16*). The peptide expressed on the virus was tested and confirmed to have binding specificity to ZnS crystal surfaces (*16, 18*). The bacteriophage containing this A7 peptide—termed A7 phage—was cloned and amplified to liquid crystalline concentrations, with DNA verification after each amplification step.

The A7 phage was precipitated and then resuspended in ZnS precursor solutions to form an A7 phage–ZnS nanocrystal (A7-ZnS) liquid crystalline suspension (*19*). The liquid crystalline behavior of the suspensions was dominated by the long-rod phage shape, despite the at-

Department of Chemistry and Biochemistry, Center for Nano- and Molecular Science and Technology, Texas Materials Institute, Institute for Cellular and Molecular Biology, University of Texas at Austin, Austin, TX 78712, USA.

*Present address: Department of Materials Science and Engineering and Biological Engineering, Massachusetts Institute of Technology, Cambridge, MA 02139, USA.

†To whom correspondence should be addressed. E-mail: belcher@mit.edu

tached ZnS nanocrystals. Polarized optical microscopy (POM) of highly concentrated A7-ZnS suspensions (127 mg/ml) showed the smectic phase (Fig. 2A). Differential interference contrast (DIC) imaging revealed 1-μm constructive and destructive interference patterns of the smectic layers (Fig. 2B). A series of successively more dilute A7-ZnS suspensions (76 to 28 mg/ml) exhibited fingerprint textures that were characteristic of the cholesteric phase (Fig. 2C), and their cholesteric pitches exponentially decayed with respect to the increase of A7-ZnS concentration. When the cholesteric suspension was placed in a magnetic field of 7.0 T for 1 hour, the cholesteric pitches were unwound and exhibited nematic phase. The phases changed under the magnetic field as a result of the diamagnetic properties of the 2700 copies of the major coat protein, pVIII, of the M13 bacteriophage (*12*). Because the pIII expresses five copies within the protein coat (less

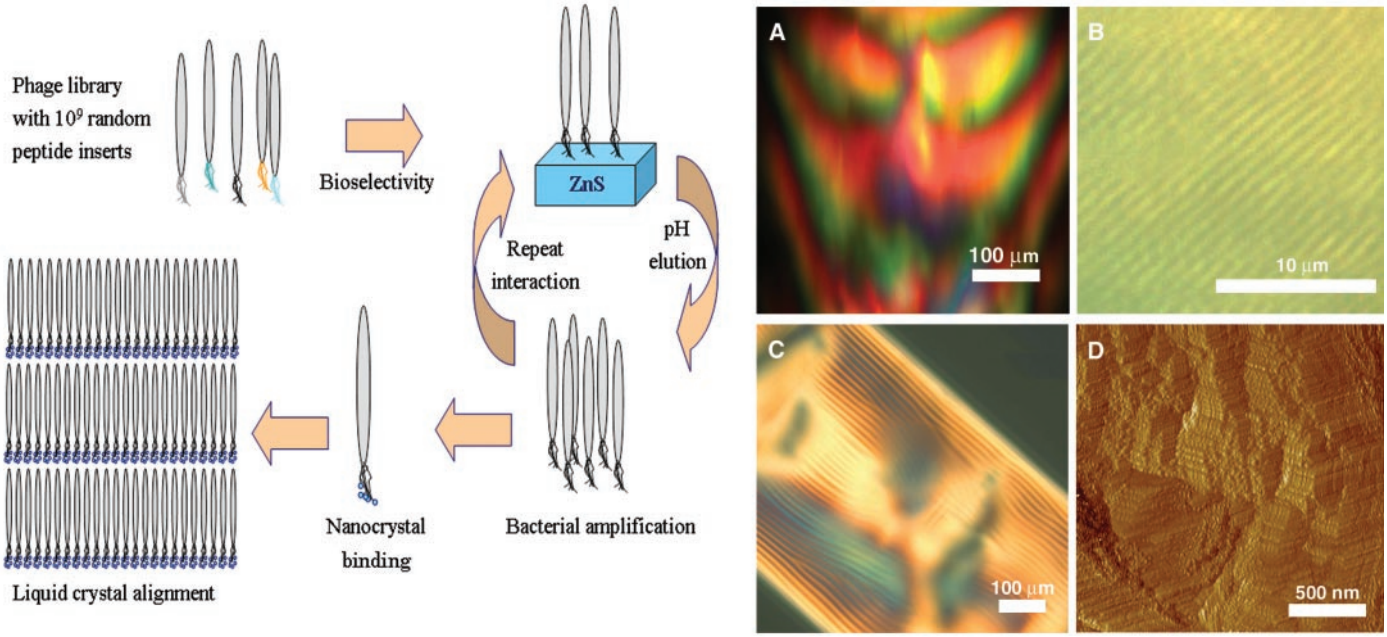

Fig. 1 (**left**). Schematic diagram of the process used to generate nanocrystal alignment by the phage display method. **Fig. 2** (**right**). Characterization of the liquid crystalline suspensions of A7 phage–ZnS nanocrystals (A7-ZnS) and cast film. (**A**) POM image of a smectic suspension of A7-ZnS at a concentration of 127 mg/ml. (**B**) A DIC filter brought out dark and bright periodic stripes (~1 μm) that show constructive and destructive interference patterns generated from parallel aligned smectic layers in the A7-ZnS suspension. (**C**) The characteristic fingerprint texture of the cholesteric phase of an A7-ZnS suspension (76 mg/ml). (**D**) AFM micrograph of a cast film from an A7-ZnS suspension (~30 mg/ml) showing close-packed structures of the A7 phage particles.

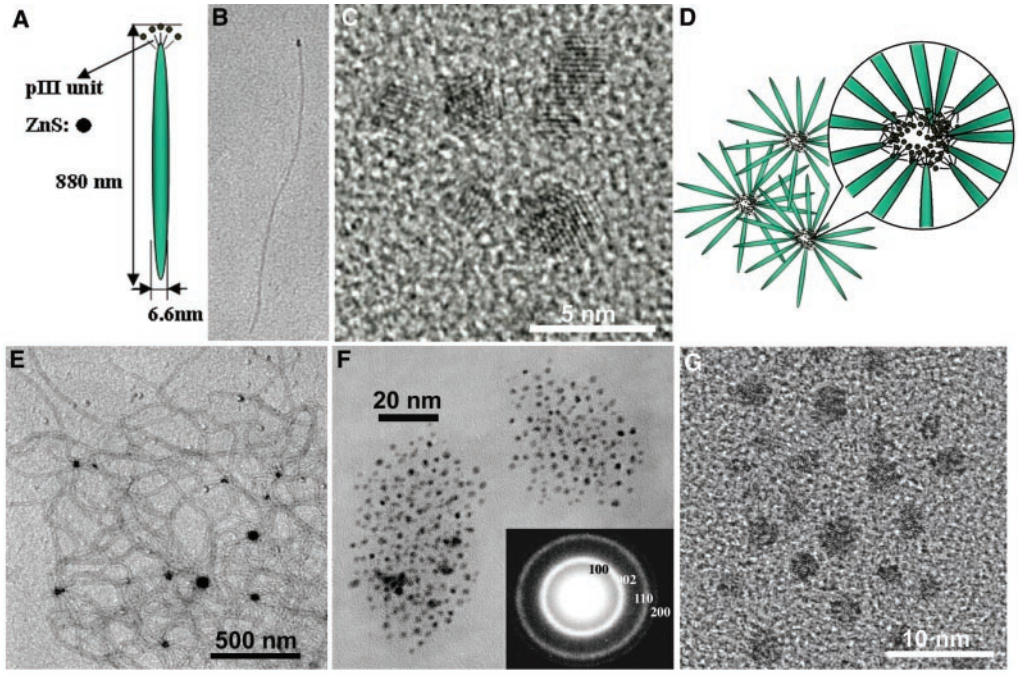

Fig. 3. Characterization of the dilute A7-ZnS suspension using TEM. (**A**) Schematic diagram of the individual A7 phage and ZnS nanocrystals. The pIII peptide unit and the ZnS nanocrystal bound to A7 phage are not drawn to scale. (**B**) TEM image of an individual A7 phage (880 nm in length) and ZnS nanocrystals, stained with 2% uranyl acetate. (**C**) High-resolution TEM image of 0.01% A7-ZnS suspension, showing lattice fringe images of five wurtzite ZnS nanocrystals. The *d* spacing of the nanocrystals was 0.22 nm, corresponding to (102) plane. (**D**) A schematic diagram of the micelle-like structures, in which ZnS nanocrystal aggregates are surrounded by A7 phage. (**E**) Low-resolution TEM image of 0.1% dilute A7-ZnS smectic suspension, showing micelle-like aggregates of ZnS nanocrystals surrounded by A7 phage after staining. (**F**) The same sample from (E) before staining shows that 100 to 150 nanocrystals formed aggregates. The inset shows a selected area electron diffraction pattern of the nanocrystal aggregates, confirming crystalline wurtzite ZnS structures. (**G**) High-resolution TEM image of 0.1% A7-ZnS suspension showing lattice fringe images of wurtzite ZnS nanocrystals. The *d* spacing of the nanocrystals was 0.22 nm, corresponding to (102) plane.

than 1%), it is implied that the ZnS nanocrystals attached at the A7 interface are following an alignment pattern dictated by the overall M13 bacteriophage alignment. The nematic phase was observed at 22 mg/ml.

A close-packed arrangement of A7 phage particles was observed from a viral-cast film on an indium tin oxide (ITO)–covered glass substrate from A7-ZnS suspensions (~30 mg/ml) using atomic force microscopy (AFM) (Fig. 2D). The average center-to-center distance of A7 phage measured ~12 nm. The A7 phage particles stood at an angle on the ITO film surface. All of the phage within ~200-nm domains had the same orientational and positional long-range ordered structure, strongly indicating a smectic B structure, in which molecules are arranged in layers with the molecular center positioned in a hexagonal close-packed array (*20*).

Both the crystal structures of ZnS nanocrystals and the individual shapes of A7-ZnS were determined using transmission electron microscopy (TEM) for a series of decreasingly dilute smectic suspensions (*21*). In the 0.01% diluted sample (Fig. 3, B and C), small-size aggregates composed of multiple ZnS nanocrystals were observed within a boundary 10 to 20 nm in diameter. The number of particles observed within the defined boundary suggested that each of the A7 phage recognized multiple nanocrystals and confined ZnS placement within the pIII subunit boundary. At higher concentrations, different types of aggregation were observed. In the 0.1% diluted sample, ~50-nm aggregates consisting of 100 to 150 nanocrystals were frequently observed (Fig. 3F). Most of the particles had a well-defined shape and were highly crystalline structures with a particle size of 2.66 ± 0.22 nm. High-resolution TEM lattice fringe imaging revealed wurtzite ZnS nanocrystals with a *d* spacing of 0.22 nm, corresponding to the (102) plane of wurtzite ZnS (Fig. 3, C and G). Selected area electron diffraction patterns confirmed the nanocrystal structure in lattice fringe images (Fig. 3F, inset). After staining the 0.1% diluted sample, A7 phage micelle-like structures appeared to surround the 50-nm ZnS nanocrystal aggregates (Fig. 3E) (*18*). This micelle-like arrangement (Fig. 3D) is most likely driven by a hybrid structure (Fig. 3A) of the A7-ZnS complex, with inorganic nanocrystals attached to organic phage. We think that the individual phage binding the nanocrystals form these structures at the concentrations used for TEM preparation. In concentrations higher than 0.1%, the phage and particles intertwined and formed thick aggregates on the TEM grid carbon film surface.

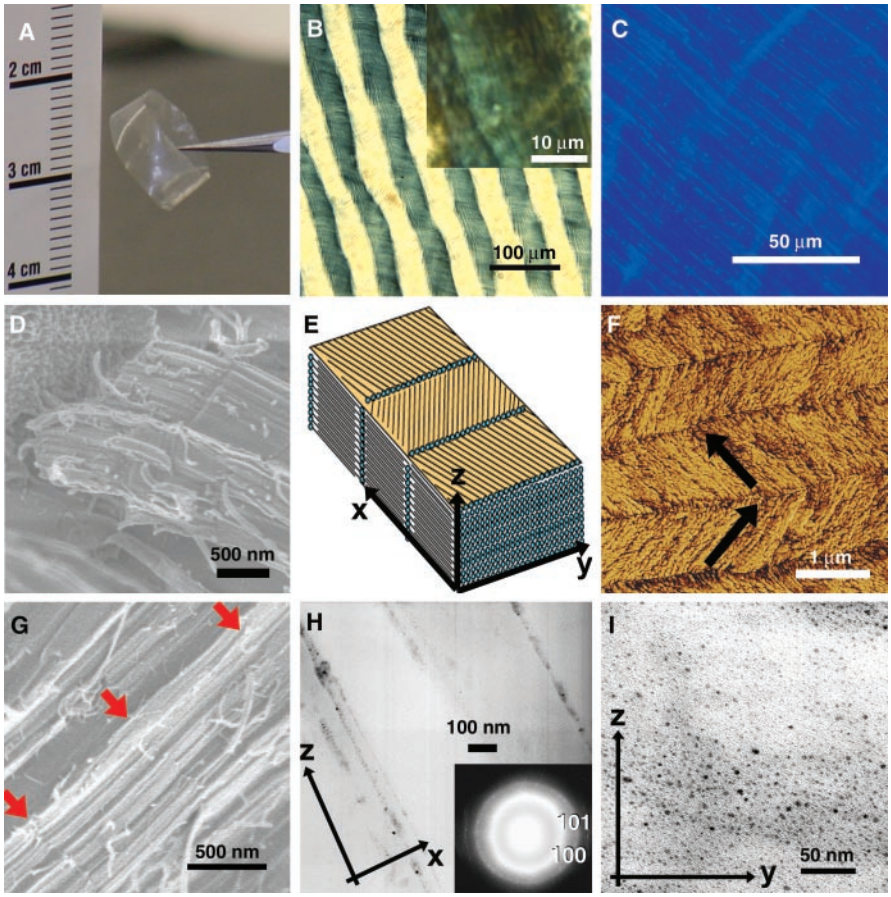

Fig. 4. Characterization of A7-ZnS film. (**A**) Photograph of A7-ZnS viral film. (**B**) POM (20×) birefringent dark and bright band patterns (periodic length 72.8 μm) were observed. These band patterns are optically active, and their patterns reverse depending on the angles between polarizer and analyzer. (**C**) Photoluminescent image, with an excitation wavelength of 350 nm and with filtering below 400 nm, shows ~1-μm stripe patterns (50×). (**D**) SEM images of highly packed three-dimensional bulk film structure. (**E**) Schematic structural diagram of the A7-ZnS composite film. (**F**) AFM image of the free surface. The phage forms parallel aligned herringbone patterns that have almost right angles between the adjacent director (arrows). (**G**) SEM image showing the close-packed lamellar structure of phage and nanocrystal layers (red arrows) in the inner areas of the film. (**H**) Low-resolution TEM image of cross section of A7-ZnS film, with 20 nm × 2 μm ZnS nanocrystal stripe pattern aligned between one phage length in the *x*-*z* direction of film; the inset shows an electron diffraction pattern of ZnS wurtzite structure. (**I**) Low-resolution TEM image of film viewed in the *y*-*z* direction, showing ZnS nanocrystals.

Highly ordered A7-ZnS self-supporting viral films (Fig. 4A) were prepared from an isotropic phase of bacteriophage and ZnS precursor solutions (*22*). The viral nanocrystal hybrid film was transparent and easily manipulated with forceps. Isotropic liquid crystalline phase concentration (~5 mg/ml) was chosen for better ZnS nanocrystal mobility in A7 phage concentrated suspension media, coupling, and self-assembly. The films were typically ~15 μm thick and several centimeters in extent. The surface viral morphology was smectic O; the interior morphologies were smectic A and C. The ordered morphologies of the viral film were characterized by POM, scanning electron microscopy (SEM), TEM, and AFM.

Optical characterization revealed that the films were composed of ~72-μm periodic domains that had smectic layer structures within the domain boundaries (Fig. 4B). With the use of high-resolution SEM, we could see the spacing of periodic layers of both the phage and ZnS nanocrystals (*23*). The films showed smectic-like lamellar morphologies between the ZnS nanocrystals and A7 phage layers (Fig. 4G). The periodic length (895 nm) corresponded to that of the bacteriophage (880 nm) and nanocrystal aggregates (~20 nm). The average size of the nanocrystal aggregates in the film was ~20 nm, as observed in the TEM of individual virus particles with nanocrystals. Microtomed 50-nm cross sections of a viral film showed nanocrystals 2 to 3 nm in diameter that were aligned ~20 nm in width and extended to more than 2 μm in length (*24*). The 2 μm by 20 nm bands formed in parallel and were separated by ~700 nm. This spacing, shorter than the expected distance (M13 phage length = 880 nm), corresponds to the length scale imposed by the phage, which formed the tilted smectic alignment of the phage with respect to layer normal.

AFM observation of free surface orientation of the A7-ZnS film (Fig. 4F) showed that the phage formed parallel aligned smectic O herringbone patterns. Phage particles had long-range orientational ordering that was persistent

over many micrometers. Inorganic ZnS nanocrystals were confined at junction areas where two adjacent lamellar layers met. Fluorescent imaging of the film (Fig. 4C) exhibited a pattern of ~1 μm fluorescent lines, corresponding to the ZnS nanocrystals arranged in the film. In a control viral film, without ZnS crystals, no fluorescence was observed (*18*). Because freely suspended liquid crystalline films form highly ordered structures on the free surface as a result of surface forces (*25*), smectic O herringbone patterns on the film surface might have higher order than the smectic A or smectic C within inner areas in this film. The observed smectic O morphology of the A7-ZnS film is similar to the high-ratio rod-coil ($f_{\text{rod-coil}} > 0.96$) block copolymers, which favor the bilayered and interdigitated morphologies (*6*). This similarity to A7-ZnS structure ($f_{\text{phage-nanocrystals}} = \sim 0.98$) strongly suggests that the A7-ZnS might have interdigitated morphology, where the director (bacteriophage axis) flips by 180° between adjacent A7-ZnS particles in the film. Considering the packing free energy, the interdigitated structure might be the most stable structure for the particles having a larger head (20-nm nanocrystal aggregates) and extremely long rod tail particles (Fig. 3, A and B). A schematic diagram of the A7-ZnS film is shown in Fig. 4E.

The mechanism for the formation of self-assembled smectic-like lamellar structure of the A7-ZnS film is still being investigated. The morphologies we observe in the film are similar to the results of earlier experiments and theoretical work on rigid and flexible block copolymers (*6, 26*). The A7 phage recognize and physically bind ZnS nanocrystals, preventing macro phase separation into separate organic and inorganic blocks. As the solvent is gradually removed, the virus particles develop orientational order within the suspension and the smecticlike lamellar structure begins to grow from several nucleation points. The mesomorphic structure in the suspension is retained even after the complete evaporation of the solvent and forms the highly ordered self-supporting viral film.

Our approach to aligning nanocrystals in a genetically engineered phage-based liquid crystal system has several advantages. Monodisperse biopolymers of specified lengths (A7 phage) can be easily prepared by molecular cloning techniques. By genetic selection of a peptide recognition moiety, one can easily modulate and align different types of inorganic nanocrystals in 3D layered structures (*27*). Additionally, we have found that the viral films can be stored at room temperature for at least 7 months without losing the ability to infect a bacterial host and with little loss of titer. This finding indicates that the fabrication of viral film is a reversible process. Moreover, we believe that the film fabrication may constitute a new process for storage of high-density engineered DNA. We anticipate that our approach, using recognition as well as a liquid crystalline self-ordering system of engineered viruses, may provide new pathways to organize electronic, optical, and magnetic materials.

References and Notes

1. J. P. Mathias, E. E. Simanek, G. M. Whitesides, *J. Am. Chem. Soc.* **116**, 4326 (1994).
2. X. Duan, J. Wang, C. M. Lieber, *Appl. Phys. Lett.* **76**, 1116 (2000).
3. D. J. Norris, M. G. Bawendi, *Phys. Rev. B* **53**, 16347 (1996).
4. C. E. Fowler, W. Shenton, G. Stubbs, S. Mann, *Adv. Mater.* **13**, 1266 (2001).
5. S. M. Yu *et al.*, *Nature* **389**, 167 (1997).
6. J. T. Chen, E. L. Thomas, C. K. Ober, G.-P. Mao, *Science* **273**, 343 (1996).
7. T. Douglas, M. Young, *Nature* **393**, 152 (1998).
8. A. P. Alivisatos *et al.*, *Nature* **381**, 56 (1996).
9. C. A. Mirkin, R. L. Letsinger, R. C. Mucic, J. J. Storhoff, *Nature* **382**, 607 (1996).
10. P. V. Braun *et al.*, *J. Am. Chem. Soc.* **121**, 7302 (1999).
11. Z. Dogic, S. Fraden, *Phys. Rev. Lett.* **78**, 2417 (1997).
12. _____, *Langmuir* **16**, 7820 (2000).
13. J. Lapointe, D. A. Marvin, *Mol. Cryst. Liq. Cryst.* **19**, 269 (1973).
14. S. A. Issaenko, S. A. Harris, T. C. Lubensky, *Phys. Rev. E* **60**, 578 (1999).
15. S. R. Whaley, D. S. English, E. L. Hu, P. F. Barbara, A. M. Belcher, *Nature* **405**, 665 (2000).
16. C. E. Flynn, C. Mao, J. L. Williams, B. A. Korgel, A. M. Belcher, in preparation.
17. C. Mao, C. E. Flynn, A. M. Belcher, in preparation.
18. Supplementary data are available on *Science* Online at www.sciencemag.org/cgi/content/full/296/5569/892/DC1.
19. The highest concentration of A7-ZnS suspension was prepared by adding 20 μl of 1 mM $ZnCl_2$ and Na_2S solutions, respectively, into the ~30 mg of phage pellet after centrifugation. Various A7-ZnS suspensions were prepared by diluting the smectic A7-ZnS suspensions. Their concentrations were measured by ultraviolet absorption spectroscopy at 269 nm. These suspensions were transferred to cover slips and 0.7-mm glass capillary tubes and characterized.
20. G. W. Gray, J. W. G. Goodby, *Smectic Liquid Crystals* (L. Hill, Glasgow, 1984), pp. 23–44.
21. One drop of dilute suspension was applied to a TEM grid, washed with distilled water, and quickly dried. Some samples were stained with 2% uranyl acetate to observe bacteriophage.
22. Bacteriophage pellets were suspended with 400 μl of tris-buffered saline (TBS, pH 7.5) and 200 μl of 1 mM $ZnCl_2$ to which 1 mM Na_2S was added. After rocking for 24 hours at room temperature, the suspension, which was contained in a 1-ml microcentrifuge tube, was slowly dried in a dessicator for 1 week.
23. A7-ZnS films were observed by SEM. For SEM analysis, the film was fractured, then coated via vacuum deposition with 2 nm of chromium in an argon atmosphere.
24. The film was embedded in epoxy resin (LR white) for 1 day and polymerized by adding 10 μl of accelerator (London Resin Co. Ltd.). After curing, the resin was thin-sectioned with a Leica Ultramicrotome; ~50-nm sections were floated on distilled water and picked up on blank gold grids.
25. A. A. Sonin, N. Clark, *Freely Suspended Liquid Crystalline Films*, (Wiley, New York, 1998), pp. 25–43.
26. N. Semenov, S. V. Vasilenko, *Sov. Phys. JETP* **63**, 70 (1986).
27. Although our liquid crystal systems have only incorporated ZnS at present, our group has already selected phage with specific peptide recognition to, and nucleation control of, many materials including II-VI semiconductor crystal surfaces (CdS, PbS, CdSe, ZnSe) and other magnetic materials. Therefore, liquid crystal systems using these and other materials are possible and currently being investigated.

28. We thank J. Williams for assistance in amplifying the clones, J. Mendenhall for assistance in preparation of samples for TEM, J. Ni for assistance in AFM analysis for the cast film, and D. Margolese and E. Ryan for assistance in manuscript editing. The Core TEM and SEM Facilities were used in the Texas Materials Institute, the Center for Nano- and Molecular Science and Technology, and the Institute for Cellular and Molecular Biology. Supported in part by the Army Research Office (Presidential Early Career Award in Science and Engineering), NSF (Nanoscale Interdisciplinary Research Teams), and the Welch Foundation.

14 November 2001; accepted 20 March 2002

Interpretation of Recent Southern Hemisphere Climate Change

David W. J. Thompson[1]* and Susan Solomon[2]

Climate variability in the high-latitude Southern Hemisphere (SH) is dominated by the SH annular mode, a large-scale pattern of variability characterized by fluctuations in the strength of the circumpolar vortex. We present evidence that recent trends in the SH tropospheric circulation can be interpreted as a bias toward the high-index polarity of this pattern, with stronger westerly flow encircling the polar cap. It is argued that the largest and most significant tropospheric trends can be traced to recent trends in the lower stratospheric polar vortex, which are due largely to photochemical ozone losses. During the summer-fall season, the trend toward stronger circumpolar flow has contributed substantially to the observed warming over the Antarctic Peninsula and Patagonia and to the cooling over eastern Antarctica and the Antarctic plateau.

The atmosphere of the SH high latitudes has undergone pronounced changes over the past few decades. Total column ozone losses have exceeded 50% during October throughout the 1990s (*1–3*), and the Antarctic ozone "hole" reached record physical size during the spring of 2000 (*4*). The lower polar stratosphere has cooled by ~10 K during October-November since 1985 (*5*, *6*), and the seasonal breakdown of the polar vortex has been remarkably delayed: from early November during the 1970s to late December during the 1990s, in both the